Applied Materials Today 30 (2023) 101720

Contents lists available at ScienceDirect

Applied Materials Today

journal homepage: www.elsevier.com/locate/apmt

Rapid, autonomous high-throughput characterization of hydrogel rheological properties via automated sensing and physics-guided machine learning

Junru Zhang [a], Yang Liu [a,b], Durga Chandra Sekhar.P [c], Manjot Singh [a], Yuxin Tong [a], Ezgi Kucukdeger [a], Hu Young Yoon [b], Alexander P. Haring [a,b], Maren Roman [b,d], Zhenyu (James) Kong [a], Blake N. Johnson [a,b,e,f,*]

[a] Grado Department of Industrial and Systems Engineering, Virginia Tech, Blacksburg, VA 24061 USA
[b] Macromolecules Innovation Institute, Virginia Tech, Blacksburg, VA 24061 USA
[c] Department of Computer Science, Virginia Tech, Blacksburg, VA 24061 USA
[d] Department of Sustainable Biomaterials, Virginia Tech, Blacksburg, VA, 24061, USA
[e] Department of Materials Science and Engineering, Virginia Tech, Blacksburg, VA 24061 USA
[f] Department of Chemical Engineering, Virginia Tech, Blacksburg, VA 24061 USA

ARTICLE INFO

Keywords:
High-throughput experimentation
MEMS
Sensors
Science-informed machine learning
Materials genome Initiative

ABSTRACT

High-throughput characterization (HTC) of composition-process-structure-property relations is essential for accelerating molecular and material discovery and manufacturing paradigms. Here, we present a rapid, autonomous method for HTC of hydrogel rheological properties in well plate formats via automated sensing and physics-guided supervised machine learning. The novel HTC method facilitates rapid, autonomous characterization of hydrogel rheological properties and percolation processes associated with gelation and network interpenetration in 96-well plate formats at a rate of 24 s/sample (70 times faster than the state-of-the-art). Viscoelastic properties and phase behavior obtained by the method were benchmarked against traditional rheology studies. The speed and utility of the method were demonstrated by high-resolution characterization of the gel point of Pluronic F127, collagen, and alginate-PNIPAM hydrogels in 96-well plate formats at resolutions of 0.31 wt% (Pluronic F127), 0.031 mg/ml (collagen), and 0.069 wt% (NIPAM), respectively. Experimental composition-property relation data generated from sensor multivariate time-series data, calibration data, and fluid-structure interaction models enabled accurate classification of sample phase using supervised machine learning. Feature augmentation using sensor physics, here, a fluid-structure interaction model, improved material (i.e., sample) phase classification accuracy relative to that obtained in the absence of physics-based feature augmentation. Ultimately, creating rapid, autonomous HTC methods that synergize with common high-throughput experimentation formats, such as well plates, can accelerate the pace of research across several disciplines as well as generate new tools for quality assurance and control across emerging industries.

1. Introduction

The Materials Genome Initiative (MGI) has established a new standard for accelerated molecular and materials discovery workflows through integrated autonomous, and often iterative, modeling, synthesis, and characterization loops [1,2]. While considerable efforts have been made in high-throughput synthesis (HTS), characterization remains a bottleneck and limits progress in modeling and synthesis domains. For example, it remains a challenge to rapidly screen the properties of material libraries and generate experimental data for model validation. Thus, creating rapid high-throughput characterization (HTC) methods is critical for realizing accelerated molecular and materials discovery paradigms, such as those based on high-throughput experimentation (HTE) methods (e.g., additive manufacturing-driven) [3].

Similar to HTC for molecular discovery applications, which requires characterization of various molecular characteristics and properties, including concentration, conformation, and binding affinity, HTC for

* Corresponding author.
E-mail address: bnj@vt.edu (B.N. Johnson).

https://doi.org/10.1016/j.apmt.2022.101720
Received 27 June 2022; Received in revised form 24 November 2022; Accepted 10 December 2022
Available online 23 December 2022

material discovery applications is particularly challenging given the large number of potential properties that may serve as measures of material quality (i.e., performance) [4]. HTE workflows for accelerated materials discovery, which consist of integrated HTS and HTC processes, are now emerging in accelerated photovoltaics [5] and solar fuels [1,6,7] applications. However, while considerable progress has been made for integrated and thin-film materials applications, there remains a significant demand for accelerated soft materials and biomaterials paradigms [3,8]. While various HTS platforms, such as those based on microextrusion 3D printing processes, are now available for formulating soft material libraries (e.g., hydrogel libraries), HTC of product quality remains a challenge and bottleneck. For example, accelerated soft materials discovery workflows may require HTC of mechanical [9] and transport properties as well as phase behavior and swelling response [7]. In addition, HTC formats should also synergize with existing HTS formats, particularly well plate formats, which are extensively used [3].

Hydrogels are essential soft materials for tissue engineering, drug delivery, and regenerative medicine [10]. Multiple HTE-based workflows have been recently established for accelerated hydrogel materials research [7,11,12]. To date, hydrogel HTC methods are typically based on transducer arrays or robotically-directed transducers capable of measuring composition, structure, or property data [7,13–15]. The majority of studies have adapted analytical methods, such as UV-vis spectroscopy and X-ray diffraction, for HTC of hydrogel properties. For example, a HTE-based method for optimization of injectable hydrogels for protein delivery in a 96-well plate format was recently created based on HTC of POEGMA hydrogel precursor composition, ovalbumin release kinetics using ultraviolet-visible (UV-Vis) spectroscopy and hydrogel compressive modulus and volume change using a commercially-available micromechanical tester from 22 to 40 ℃ [7]. In another study, a HTE-based method for screening PEGDA-based materials for inkjet printing in a 96-well plate format was recently established based on the characterization of ink viscosity via online pressure sensing and HTC of surface tension based on image analysis from 25 – 60 ℃ [12]. A HTE-based method for supramolecular gels research was recently established based on HTC of material optical properties via UV-Vis spectroscopy using a microplate reader format [11]. HTC of gel structure was characterized by UV-Vis absorbance measurements in a 384-well plate format from 20 – 35 ℃. Optical density measurements and fluorescence spectroscopy measurements were also used to characterize gel formation and uniformity. While emerging HTE workflows for hydrogel materials research have primarily employed HTC methods based on existing spectroscopic methods and mechanical testing platforms, there remains a need for sensor-based methods that facilitate combinatorial screening of soft material composition-structure-property data.

Among the properties of hydrogels, rheological properties are indicators of processability, performance, and quality for applications. Hydrogel rheological properties and phase behavior provide important information regarding material processability in extrusion applications, such as the ability to form free-standing structures. The viscoelastic properties of hydrogel-based tissue scaffolds are also indicators of cell behavior and phenotype in 3D cell culture models [16,17]. Thus, new methods for HTC of hydrogel rheological properties and phase behavior that synergize with practical HTE formats (e.g., well plate-based) could eliminate significant bottlenecks to accelerated soft materials research and discovery.

The gold-standard methods for characterizing hydrogel mechanical properties are rheometers, dynamic mechanical analyzers, and atomic force microscopes [18]. However, such techniques are often destructive and involve time-intensive tests (~ 0.5 – 1 day/sample) because of required manual sample preparation steps and data analysis [19], which limits throughput and potential for online product-process monitoring applications. For example, while 3D bioprinting processes now enable automated high-throughput fabrication of 3D cell culture models [1,2,9], HTC of bioink and tissue construct rheological properties remains a bottleneck to scalable and quality-controlled additive biomanufacturing. Micro-mechanical testing techniques based on miniaturized transducers, such as nanoindentation, micro-tensile testing, micro-compression testing, and micro-electromechanical systems (MEMS), now facilitate combinatorial HTC of thin-film and bulk material mechanical properties [9]. While nanoindentation is widely used, it may overestimate material properties due to size dependence [20–22]. MEMS have received considerable attention as a platform technology, such as for chemical sensing, biosensing, and material property sensing applications, based on their sensitivity, design flexibility (e.g., form factor), and ability to perform continuous monitoring. MEMS have also enabled the characterization of soft material viscoelastic properties based on fluid-structure interaction effects [23], as well as real-time monitoring of hydrogel gelation processes. Thickness shear mode resonators, such as quartz crystal microbalances (QCM) [24], were among the first MEMS leveraged for characterizing the viscoelastic properties of hydrogel thin films, which remain an active area of research [25]. Suspended micro-beams were also previously used to characterize the viscoelastic properties of hydrogel microstructures (PEGDA) [26]. However, not all MEMS exhibit versatile form factors and transduction approaches that synergize with practical HTS formats, such as well plates. For example, the form factors associated with QCM and double-clamped beam resonators are relatively more difficult to implement in robotically-directed well plate-based measurement formats. We recently showed that dynamic-mode piezoelectric milli-cantilever (PEMC) sensors, which exhibit a dip-stick form factor [27], enable the characterization of hydrogel viscoelastic properties with a sensitivity of 90 Pa (per unit quality factor) [28,29] and control of hydrogel structure and viscoelastic properties [30]. Thus, the high sensitivity, dip-stick form factor, self-exciting and -sensing transduction principle, spectral data structure, and submersion-based measurement format of PEMC sensors make them potentially attractive characterization tools for autonomous HTC of hydrogels in well plate formats.

Here, we introduce a rapid, autonomous method for HTC of hydrogel rheological properties based on the integration of robotically-directed sensing using PEMC sensors and physics-guided machine learning. The method is compatible with standard well plates and exceeds the cycle rates of state-of-the-art and gold-standard characterization methods by more than one order of magnitude. Feature augmentation using knowledge of sensor physics, here, a fluid-structure interaction model, improved the accuracy of classifying the sample's phase as a solution or gel relative to that obtained in the absence of physics-based feature augmentation. The HTC method was validated by characterizing gelation and percolation processes in several hydrogel libraries (i.e., batches of samples of known composition but unknown properties). The ability of this method to synergize with common HTE formats, such as those based on well plates, can accelerate the pace of research across several disciplines as well as generate new tools for quality assurance and control across emerging industries.

2. Materials and methods

2.1. Materials

Pluronic F127 (PF127), collagen solution from bovine skin (3 mg/ml), 10X phosphate-buffered saline, sodium hydroxide, alginate acid sodium salt from brown algae (alginate), N-isopropylacrylamide (NIPAM), and calcium chloride were from Sigma Aldrich.

2.2. Sensor fabrication

Piezoelectric milli-cantilever (PEMC) sensors with asymmetric anchoring were fabricated from lead zirconate titanate (PZT) chips (5 × 1 × 0.127 mm^3) as previously reported [31–37]. Briefly, 30-gauge copper (Cu) wires were soldered to the top and bottom thin-film nickel electrodes at the end of the PZT chip. The soldered end of the

chip was then potted in a 6 mm diameter glass tube with a non-conductive epoxy resulting in a cantilever geometry (length (L) = 4.1 mm, width (w) = 1 mm, thickness (t) = 127 μm). Anchor asymmetry was obtained by applying additional epoxy to one side of the cantilever extending from the embedded end. The sensors were then spin-coated with polyurethane (~30 μm). Subsequently, the sensors were insulated by a chemical vapor deposited Parylene C coating (10 μm) in batches of 25 - 50 sensors following vendor-supplied protocols (PDS 2010 Labcoter® 2, Specialty Coating Systems, Indianapolis, IN).

2.3. Sensor measurement principle and data acquisition

The electrical impedance-based self-sensing and -exciting actuation and transduction principle of PEMC sensors [36,38,39] enables *in situ* real-time monitoring of viscous and viscoelastic materials, such as hydrogels. While resonance of micro- and nano-cantilevers is highly damped in viscous and viscoelastic materials based on consideration of the cantilever Reynolds number, resonance monitoring of milli-cantilevers is possible in many materials since $Re_c > 1$ [33,40]. Continuous monitoring of the PEMC impedance and phase angle responses (i.e., impedance spectra) was performed using electrical impedance spectroscopy across a frequency range of ± 20-30 kHz centered on the resonant frequency (f) using a network analyzer (E5061B; Keysight). A custom MATLAB program provided simultaneous instrument (analyzer) control and real-time data acquisition. This enabled continuous monitoring of multivariate PEMC sensor responses, which included f, the phase angle at resonance (ϕ), and the impedance at resonance (Z) as described in our previous reports [31–37]. The quality factor (Q) was calculated as $Q = f$/frequency-width-at-half-maximum (FWHM).

2.4. HTC of Hydrogel rheological properties in well plates via robotically-directed sensing

The HTC platform was composed of a PEMC sensor, network analyzer, desktop computer for analyzer control and data acquisition, three-axis robot (MPS50SL; Aerotech), motion controller (A3200; Aerotech), and a desktop computer for robot control and path planning. Well plates were characterized on a custom plate holder and stage (Thorlabs) that enabled manual leveling. Leveling was achieved using a 1D laser displacement sensor (IL-1000; Keyence).

2.5. Path planning

The sensor path across the well plate (material library), known as the toolpath, was defined using G code and manual path planning based on well-reported 96-well plate dimensions. The sensor path was based on a move-dip-dwell-retract loop that resulted in the characterization of the material in each well of a given plate. The sensor moved in the direction of increasing well number, which corresponded to increasing polymer concentration based on the plate preparation protocol. The sensor responses were allowed to stabilize in air prior to all studies. The dip motion command resulted in full submersion of the PEMC sensor. The duration of the dwell time was 15 s. A feed rate of 2.5 mm/s was used for all linear motion commands. Sensor data was continuously collected throughout tool motion.

2.6. Hydrogel preparation

Hydrogel 'libraries,' which refer to a batch of hydrogel samples of known composition but unknown properties, were manually formulated in commercially-available 96-well plates. *Controls:* Plates filled with only DIW and glycerol served as negative controls, respectively. *2.6.1 Formulation of Pluronic F127 Hydrogels:* Stock PF127-water solution (30 wt%) was first prepared in DIW. The stock solution was then serially diluted with DIW across the well plate, spanning the concentration of the known gel point, to form the Pluronic F127 hydrogel library. *2.6.2 Formulation of Collagen Hydrogels:* Stock collagen solution (3 mg/mL) was first serially diluted with DIW across the plate followed by the addition of 40 μl 10X PBS and 12 μl 1N NaOH to each well that contained 360 μl collagen solution. The collagen hydrogel library formed after 1 hour at room temperature. *2.6.3 Formulation of Alginate-PNIPAM Hydrogels:* Stock NIPAM solution was serially diluted with DIW across the well plate. The alginate-PNIPAM libraries were prepared by mixing 100 μl 2 wt% alginate with 300 μl NIPAM. After the library was exposed to UV light for 30 minutes (365 nm; UVGL-58), 30 μl 100 mM $CaCl_2$ was added. The library was left overnight to react. The concentration step sizes for 96-well plate studies were 0.031 - 3 mg/ml, 0.31 - 30 wt%, 0.069 – 6.67 wt% for collagen-10X PBS-1N NaOH-water, PF127-water, and alginate-PNIPAM-$CaCl_2$ mixtures, respectively.

2.7. Benchmarking of hydrogel rheological properties via traditional rheology

The low-frequency storage (G') and loss (G'') moduli of PF127 solutions (3 – 18 wt%) were acquired by frequency sweeps (1 to 100 Hz) with a strain of 50%, which was found to be within the linear viscoelastic region, using a rheometer (MCR302; Anton Paar). The PF127 hydrogels (21 – 30 wt%) were characterized by frequency sweeps (1 to 100 Hz) at low strain (1%). Solution characterization was performed using a concentric cylinder measuring system (CC27; Anton Paar) (20 ml) at 50% strain. Hydrogels were characterized using a parallel plate test fixture (PP50; Anton Paar) (3 ml) at a gap of 1 mm and 1% strain. The MCR302 was equipped with a Peltier system for temperature control.

2.8. Calculation of hydrogel rheological properties from sensor data and sensor physics

The sensor outputs of f and Q were utilized to calculate the surrounding material G' and G'' at f from the following fluid-structure interaction model [23]:

$$g_1 = \frac{\pi}{2}\frac{b_2 G''}{\omega} + \frac{\pi}{4\sqrt{2}}\sqrt{\rho}b\left[(b_1 - a_2)\sqrt{\sqrt{G'2+G''^2}+G'} + (a_2+b_1)\sqrt{\sqrt{G'2+G''^2}-G'}\right] \quad (1)$$

$$g_2 = \frac{\pi}{4}a_1\rho b^2 + \frac{\pi}{2}b_2\frac{G'}{\omega^2} + \frac{\pi}{4\sqrt{2}}\frac{\sqrt{\rho}b}{\omega}\left[(b_1 + a_2)\sqrt{\sqrt{G'2+G''^2}+G'} + (a_2 - b_1)\sqrt{\sqrt{G'2+G''^2}-G'}\right] \quad (2)$$

$$g_1 = \frac{\pi}{4}\rho b^2\omega\left(\frac{\frac{(m_c+m_A)\omega}{Q} - c_i}{\rho b^2 L\omega\frac{\pi}{4}}\right) \quad (3)$$

$$g_2 = \frac{\pi}{4}\rho b^2\left(\frac{4\mu\left(\frac{\omega_0^2}{\omega^2}-1\right)}{\pi b^2\rho}\right) \quad (4)$$

where L is the cantilever length, $\mu = \rho_c bt$ is the cantilever mass per unit length, ρ_c and t are the respective cantilever density and thickness, Q_0 and ω_o are the respective quality factor and resonant frequency in the absence of fluid damping (i.e., resonating in vacuum with only internal damping effects present), $m_c = \rho_c btL$ is the cantilever mass, $m_A = \rho\pi b^2 L\Gamma'/4$ is the added mass, Γ' is the real part of the hydrodynamic function, and $c_i = m_c\omega_o/Q_o$ is the internal damping coefficient. Due to

the scale of the cantilevers ($L = 4.1$mm), the internal damping was not negligible and was subtracted from the measured value (as described in the term c_i in Eq. 3). In calculation of c_i, ω_o and Q_0 were approximated as $\omega_o \sim 2\pi f_{n,\ air}$ and $Q_0 \sim Q_{n,\ air}$, which were reasonable assumptions as discussed in the following sections. The hydrodynamic function was approximated using the relation $\Gamma' = a_1 + a_2\delta/b$, where $\delta = (2\eta/(\rho\omega))^{1/2}$ is the thickness of the thin viscous layer surrounding the cantilever in which the velocity has dropped by a factor of $1/e$, and η is the viscosity of the fluid. Previous work has shown that Q is also strongly correlated with φ and G' in several hydrogels [28–30]. Eqs. (3) and (4) allow for solutions of g_1 and g_2 based on measurable values (ω and Q, which are related to f and φ, which are continuously monitored). These values can then be used to obtain the desired viscoelastic properties G' and G'' at the measurement frequency using Eqs. (1) and (2) and measured values of g_1 and g_2. Thus, the solution to the system of equations formed by Equations (1) – (4) provides the viscoelastic properties of the surrounding material based on the continuously-monitored cantilever sensor response [29]. Supporting details on the solution method are provided in Supporting Information.

2.9. Calculation of percolation threshold

The gel point and percolation threshold were obtained as the inflection point of a best-fit (nonlinear least squares; Microsoft Excel) sigmoidal percolation model [41] to the experimental sensor steady-state phase angle vs. polymer concentration (c) or G' obtained from sensor data and Equations (1) – (4) vs. concentration.

2.10. Physics-guided supervised machine learning

The raw phase angle data, normalized phase angle data, low-frequency G' calculated from normalized phase angle and rheometer data, and high-frequency G' calculated from resonant frequency and quality factor data and the fluid-structure interaction model served as the input features to the material phase-classification (i.e., sol-gel transition) problem. The latter feature is generated via physics-guided fusion of sensor bivariate time-series data ($f(t)$ & $\phi(t)$) using knowledge of sensor physics (i.e., Equations (1) – (4)). The two classes 0 and 1 represented solution and gel as the output, respectively. Labeling was performed based on the best-fit sigmoidal regression model. Class 0 (solution) corresponded to sigmoidal values less than 0.5, while class 1 (gel) corresponded to values greater than 0.5. The data was divided into 80% and 20% for training and testing, respectively using Stratified sampling with respect to class labels to preserve the percentage and distribution of samples in each class. Supervised machine learning was performed using Support vector machine (SVM), Random forest (RF), and Extreme gradient boosting (XGB) classifiers. Regularization parameter C in SVM, minimum trees leaf, minimum trees split, and the maximum depth of trees in random forest, and number of trees in the classifier, the maximum depth of trees, the learning rate, and subsample ratio of columns in XGB model hyperparameters were tuned for optimal results. No tuning was done to default parameter values that resulted in 100% accuracy. Additional details regarding model tuning are provided in Supporting Information. Model accuracy score, F1-score, precision, recall, and misclassification error were used to evaluate model performance. Supervised machine learning was performed using a personal computer (Linux; 12 GB RAM) and statistical software and packages (Python).

2.11. Statistical analysis

Data were expressed as mean ± standard error of the mean. Normality of the data was assessed by a normal probability (Q-Q) plot. The significance of differences between the mean values of: 1) f and ϕ in various surrounding materials; and 2) G' and G'' above and below the gel point (e.g., at the limit of high polymer concentration) were determined by Student t-tests and one-way ANOVA. Statistical analysis was performed using statistical software (Python).

3. Results and discussion

As illustrated in Fig. 1a, we report a novel rapid, autonomous method for HTC of hydrogel rheological properties in well plates based on robotically-directed sensing and supervised machine learning. Photographs of the HTC platform are provided in Supporting Fig. S1. The premise of this work is that the integration of automated (i.e., robotically-directed) sensing and machine learning provides an autonomous HTC method that can accelerate the screening of large batches of hydrogels using traditional HTE experimentation formats (well plates) relative to traditional characterization methods (see Fig. 1b). As shown in Fig. 1a and c, automated sensing of hydrogel rheological properties in well plates was performed using dynamic-mode PEMC sensors. PEMC sensors were selected given their design synergizes with well plate formats that are commonly used in HTE. In particular, the self-sensing and -exciting transduction mechanism and milli-scale dip-stick form factor supports interrogation of small sample volumes without requiring bulky supporting measurement instrumentation. The electrical impedance-based transduction mechanism also provides access to high sampling rates, which is important for achieving rapid measurement. The cantilever geometry also enables use of established sensor physics, specifically fluid-structure interaction models, for interpretation of sensor response and guidance of autonomous operations (e.g., machine learning-based classification of material properties or phase). While PEMC sensors enable rheological property sensing at different submersion depths [31], the measurements reported in this work correspond to fully submerged sensors, which enables the characterization of the material rheological properties through a fluid-structure interaction model [23] based on the sensor impedance response. As shown in Fig. 1a and c, HTC was achieved by continuous monitoring of the impedance response around the resonant frequency (f) as the sensor was robotically directed through the sample library based on a user-defined path.

Given its extensive use, we first validated the method using the well-characterized PF127-water system. As shown in Fig. 1d and e, various features of the PEMC sensor impedance response (i.e., spectral data) correlated with the polymer concentration of the PF127-water mixture across the 0 – 30 wt% range. The time to collect the 96 impedance spectra was 4 hours, which included the time associated with sensor cleaning. The dependence of the f and phase angle at resonance (ϕ) responses on the PF127 concentration are shown in Fig. 1f and g. The dependence of quality factor (Q) on ϕ is shown in Supporting Fig. S2. The largest rate of change in the steady-state ϕ response occurred at the inflection point of the sigmoidal curve (18.33 ± 0.95 wt%), which agreed well with the reported gel point for the PF127-water system at room temperature [42] (see Fig. 1g). We also found that f, ϕ, and Q were significantly different across the solution vs. gel concentration ranges ($p = 0.015$, $p < 0.001$, and $p < 0.001$, respectively, $n = 24$ data points). Previously, we showed that ϕ response correlated with low-frequency G' of gelatin and alginate hydrogels obtained by dynamic mechanical analysis [28–30]. As shown in Fig. 1h, the trends in the sensor spectral response with polymer concentration (see Fig.1f and g) also correlated with low-frequency G' (1 Hz) obtained using a rheometer. The G' and G'' ranged from 0 - 28.6 ± 1.85 and 0 - 2.62 ± 0.08 kPa ($n = 3$ repeated studies), respectively, across the 3 - 30 wt% concentration range. As shown by the location of the crossover point, the rheology studies also suggested a gel point near 20 wt% based on the crossover of G' and G'', which agrees with the transition point estimated by the trends of raw PEMC sensor spectral data. While characterization studies using a traditional rheometer enabled estimation of the gel point, the technique exhibited various disadvantages, including relatively increased sample characterization time (~30 min/sample) and sample volume (20 ml for solution; 3 ml for gel), yet still provided limited resolution of the percolation process (i.e., relatively high uncertainty in the percolation

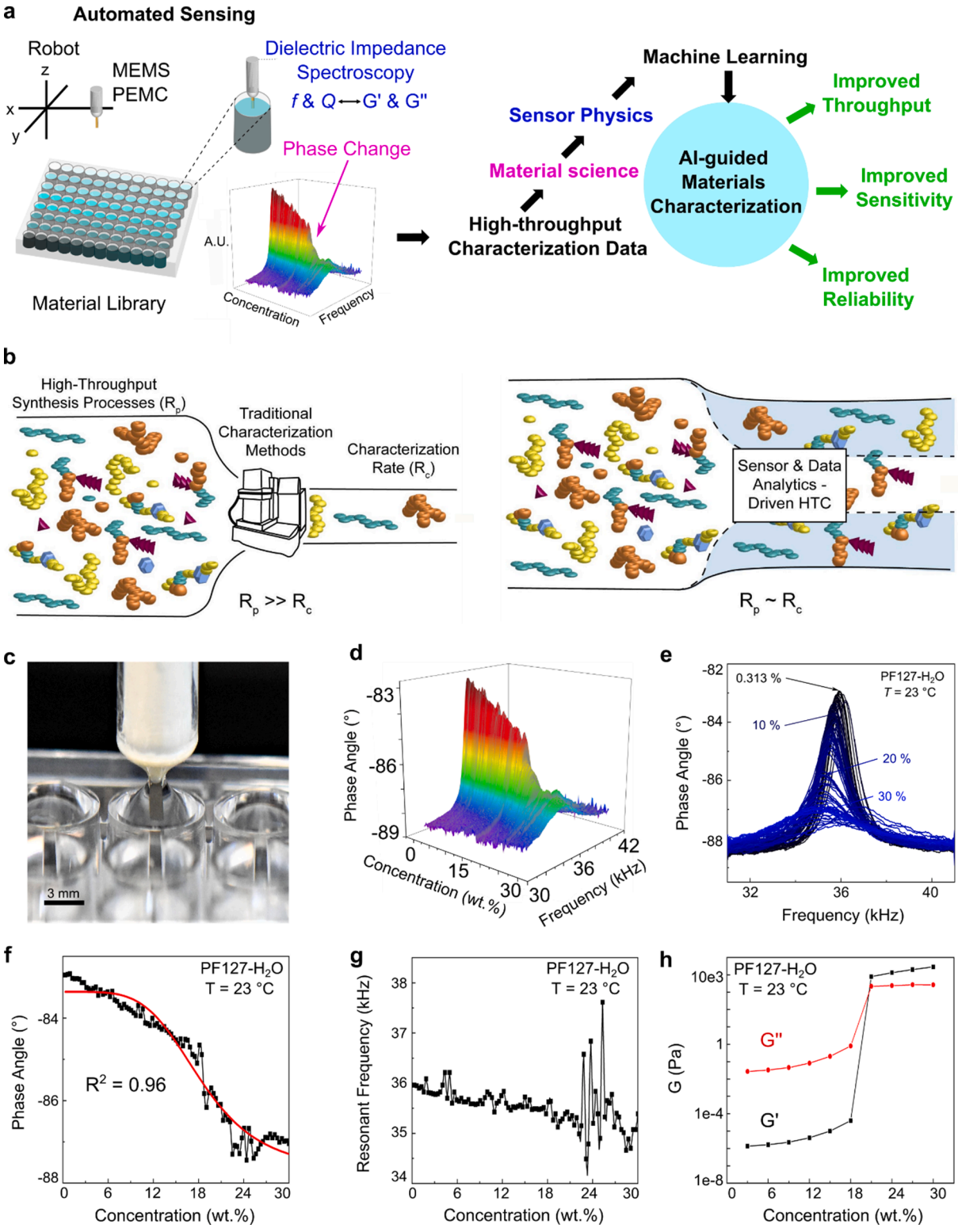

Fig. 1. a) Illustration of a rapid, autonomous method for high-throughput characterization (HTC) of hydrogel rheological properties via automated sensing and physics-guided supervised machine learning (spectra shown in arbitrary units (A.U.)). **b)** Illustration of the effect of novel autonomous sensor- and data-driven HTC methods on achievable screening throughput relative to traditional characterization processes. **c)** Photograph of dynamic-mode piezoelectric milli-cantilever (PEMC) sensor-material interaction during submersion into a well of a 96-well plate. Impedance response (i.e., resonant frequency (f) and phase angle response (ϕ)) of the PEMC sensor second mode while submerged in various PF127-water mixtures ranging from 0.31 – 30 wt% in 3D **(d)** and 2D **(e)**. Dependence of ϕ **(f)** and f **(g)** on the material PF127 concentration. **h)** Rheometer-measured low-frequency shear storage (G') and loss (G'') moduli among concentration across the 3 – 30 wt% range for the PF127-water system (error bars are not visible based on the y-axis scale)).

threshold). Thus, the integration of PEMC sensors with robotics and machine learning could potentially facilitate autonomous HTC of hydrogel rheological properties in well plate formats using small sample volumes.

Having discussed the sensor-based measurement principle associated with the characterization of hydrogel viscoelastic properties using the PF127-water system and the correlation among sensor outputs (f, ϕ, and Q) and low-frequency rheological properties obtained by traditional rheology, we next examined the ability to automate the characterization of a hydrogel library rheological properties and phase behavior in a 96-well plate reading format. Automating the characterization process via robotically-directed sensing can reduce the characterization cycle time and, therefore, average characterization time per sample by potentially decreasing the handling, operation, and tooling times associated with a characterization process. Thus, automating the characterization process is an important aspect of increasing the speed and, thus, the throughput of a characterization method. The robotically-directed sensor path and concentration distribution across the 96-well plate are shown schematically in Fig. 2a. The concentration of the PF127-water library varied linearly across the well plate from the 0.31 – 30 wt% range with a step size of 0.31 wt%.

The f and ϕ responses and corresponding rheological property heat maps associated with the library obtained from steady-state sensor responses during submersion in successive samples are shown in Fig. 2b and c. In this study, an optimized acquisition time of 15 s/sample was utilized, but the measurement time may theoretically be reduced to on the order of $1/f$ or the time constant associated with the cantilever's free response. The steady-state f response exhibited a complex trend across the 0.31 – 30 wt% PF127 concentration range. The steady-state ϕ response exhibited a sigmoidal trend with an inflection point at t = 28.58 min (see Fig. 2c), which corresponded to c = 19.375 wt% (recall that time corresponded to concentration because of the constant robot feed rate). The gel point, characterized by the inflection point of best-fit sigmoidal curve, was 18.85 ± 0.48 wt% (n = 3 repeated experiments), which agreed with a previously reported range (18 – 21 wt%) [42]. The steady-state ϕ responses before and after gelation were also significantly different ($p < 0.001$, n = 24). The results of normality testing for data associated with the solution and gel phases are provided in Supporting Fig. S3. Importantly, the features of gelation in the sensor data, such as the inflection point of the ϕ response, were absent from negative control studies with water and glycerol in which gelation was absent (see Fig. S4). It should be noted that the data acquisition, analysis, and interpretation were autonomous (i.e., based on robotics and regression) and provided a significantly higher resolution of the phase boundary than traditional methods (see Fig. 1h) but with significantly reduced time-to-results and required sample volume. The total characterization time was 37.13 min, which included 3 s associated with composition-property relation regression analysis. Thus, the method

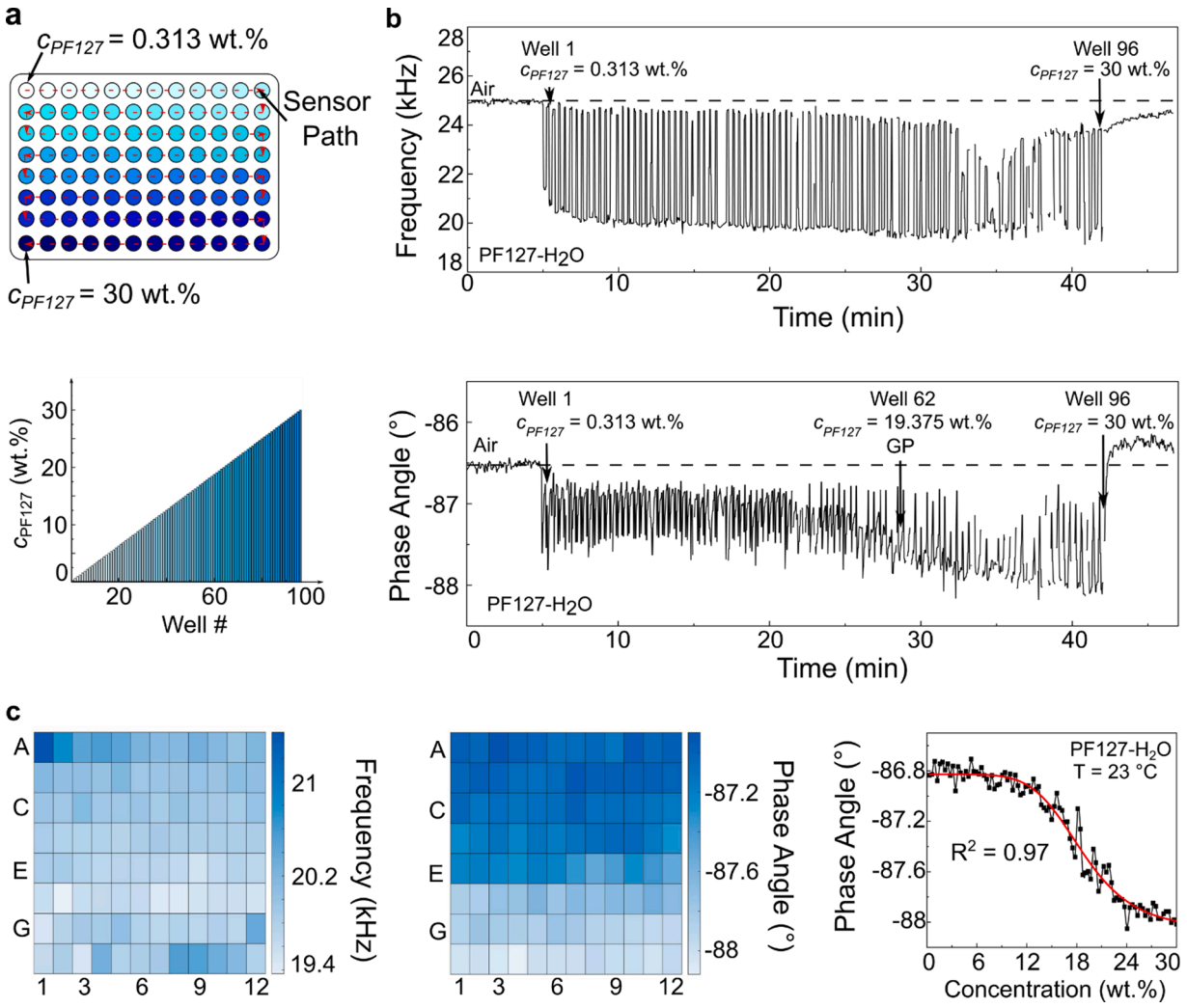

Fig. 2. **a)** Schematic of the sensor path and concentration distribution of the PF127 hydrogel library in a 96-well plate format. **b)** Sensor resonant frequency (f) and phase angle (ϕ) responses associated with the measurement. **c)** Heat maps for 96-well plate steady state sensor responses, and plot of steady-state ϕ response with respect to concentration showing the best-fit sigmoidal curve (R^2 = 0.97).

provided automated HTC at a rate of 24 s/sample, which included the time associated with sensor motion, measurement, calculation of rheological properties from sensor data via Equations (1) – (4), and regression-based identification of the gel point.

As previously discussed and illustrated in Fig. 3a, the PEMC sensor data can be used to quantify the rheological properties of each sample in the material library using the fluid-structure interaction model or based on calibration using results from traditional rheology studies (see Fig.3b). The rheological property maps associated with the hydrogel library calculated from the sensor physics (i.e., Equations (1) – (4)) are shown in Fig. 3c. The computation time was 1 s. The resultant composition-rheological property relation for the PF127-water system at room temperature is shown in Fig.3d. As shown by comparison of Figs. 3c, 3d, and 1f, the ϕ response and G' at f obtained from sensor data and physics exhibited similar magnitude to low-frequency G' and G'' values obtained using the commercially-available rheometer. In addition, G' and G'' at f also exhibited a sigmoidal trend, with an inflection point (i.e., gel point) at 19.06 wt%, which also agreed with previously reported values [42]. Similar to the ϕ response, G' and G'' were significantly different before and after gelation ($p < 0.001$ and $p < 0.001$, respectively; $n = 24$).

Fig. 3e shows the strong correlation between the normalized steady-state ϕ response ($= [\phi - \phi_i]/[\phi_f - \phi_i]$) and the low-frequency viscoelastic properties obtained using a rheometer. The normalized ϕ response also exhibited a sigmoidal trend with an inflection point at 19.06 wt%. Fig. 3f shows a comparison of the low-frequency G' obtained using normalized ϕ response and results from the traditional rheometer studies with the G' at f (i.e., obtained from sensor physics). As shown in Fig. 3f, G' at f was lower in magnitude than at low frequency yet exhibited a similar dependence on concentration, with inflection points at 19.06 wt%, respectively. The calibration-based method for rheological property characterization offers the advantage of incorporating benchmarking data from traditional characterization methods (e.g., rheometers), but the disadvantage of requiring additional time associated with such

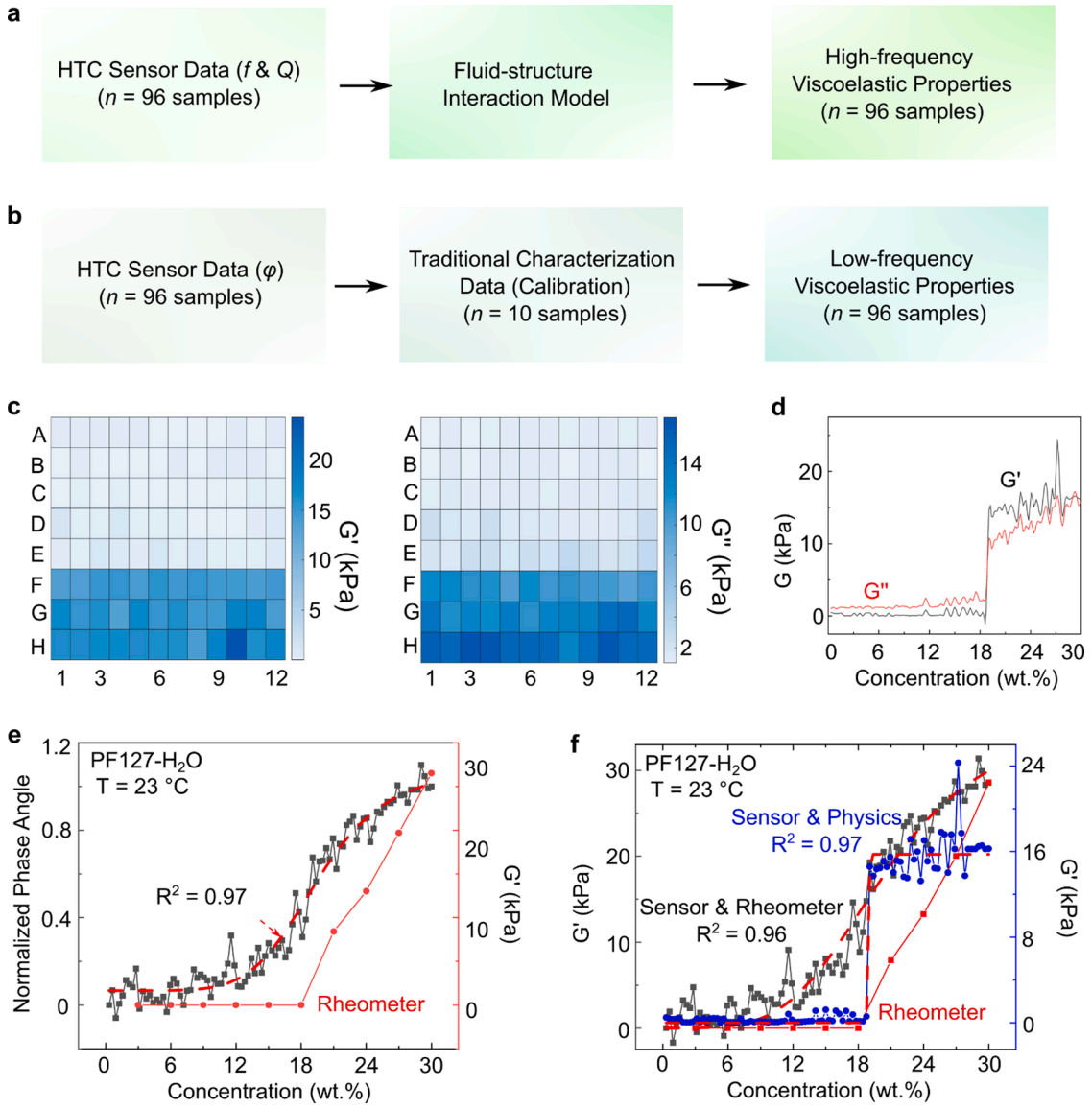

Fig. 3. a) Workflow of composition-property relation data generated from sensor data and physics. **b)** Workflow of composition-property relation data generated from sensor data using calibration-based approach. **c)** Rheological property heat maps of storage (G') and loss (G'') moduli generated from sensor data and physics. **d)** Composition-property relations corresponding to the heat maps shown in panel **(c). e)** Normalized steady-state ϕ response, best-fit sigmoidal regression model, and low-frequency G' measured from rheometer with respect to concentration. **f)** The composition-property relations from ϕ response and rheometer calibration data and best-fit sigmoidal curve, low-frequency rheometer data, and G' from sensor resonant frequency (f) and quality factor (Q) responses using a fluid-structure interaction model (i.e., sensor physics) and best-fit sigmoidal curve.

studies if data were not pre-existing. The sensor- and physics-based method for rheological property characterization has the advantage of relatively increased characterization rate, as it avoids the need for traditional characterization methods. Both approaches provide equivalent resolution and throughput in the case of pre-existing calibration data.

In addition to formulating hydrogel libraries that exhibit a linear change in composition across the plate, we also verified that the method was capable of resolving nonlinear and discontinuous changes in sample concentration as well as successive phase changes along the sensor path.

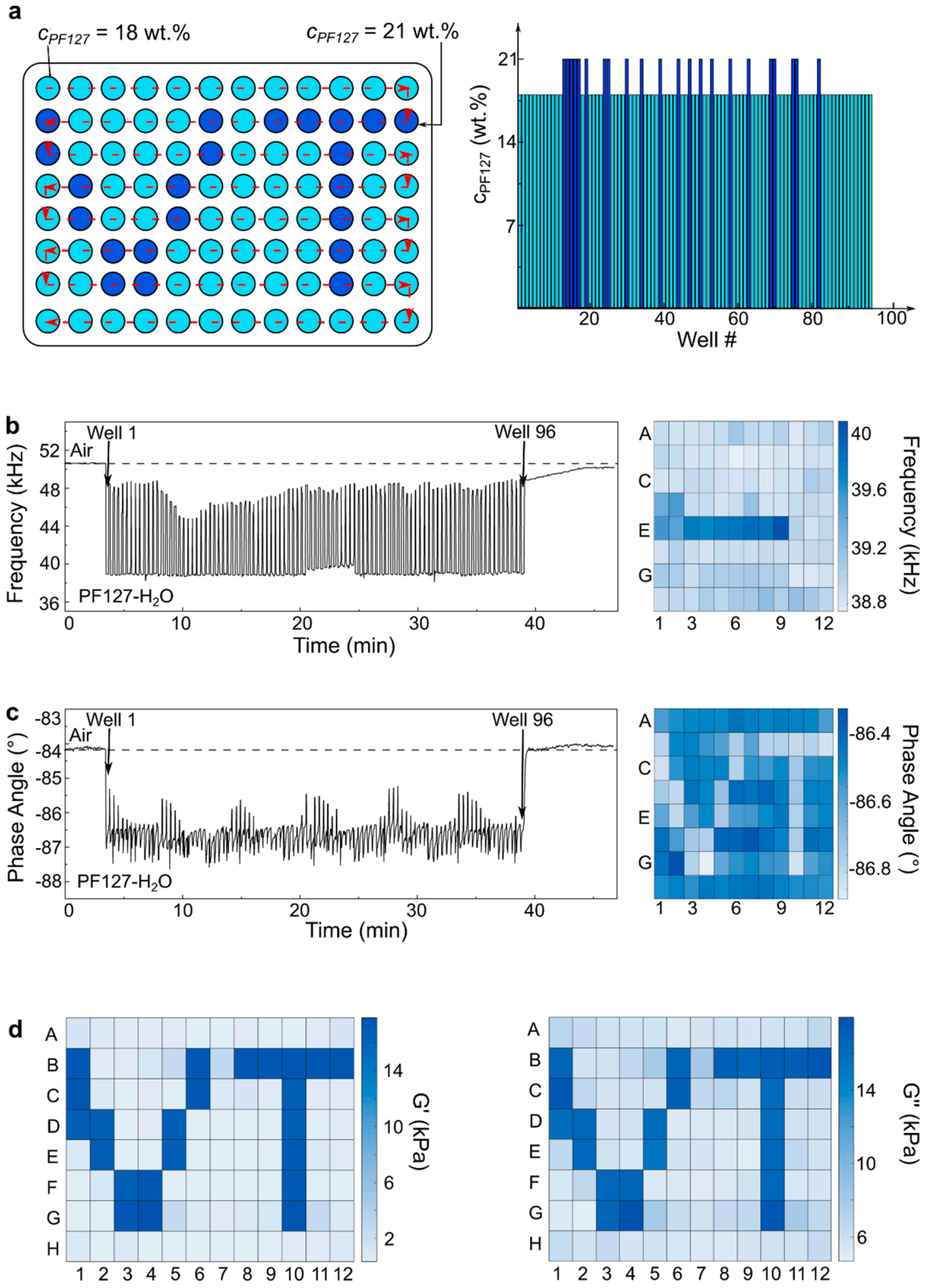

Fig. 4. **a)** Schematic of the sensor path and concentration distribution of the PF127 hydrogel library in a 96-well plate format. Sensor resonant frequency (f) **(b)** and phase angle (ϕ) **(c)** responses associated with the measurement and corresponding heat maps. **d)** Rheological property heat maps of storage (G') and loss (G'') moduli generated from sensor data and physics.

For example, such libraries may be found in chemical sensing and biosensing applications in which sample concentration may be unknown and spatially uncorrelated across the plate. As shown in Fig. 4a, we characterized a library that contained two PF127-water mixtures, one below (18 wt%) and one above (21 wt%) the gel point at room temperature. The concentration exhibited a Virginia Tech "VT"-shaped spatial distribution across the 96-well plate (Fig. 4a). The f and ϕ responses and corresponding heat maps of steady-state responses during submersion are shown in Fig. 4b and c. As shown in Fig. 4d, the "VT" distribution can be observed in the viscoelastic property heat maps. In

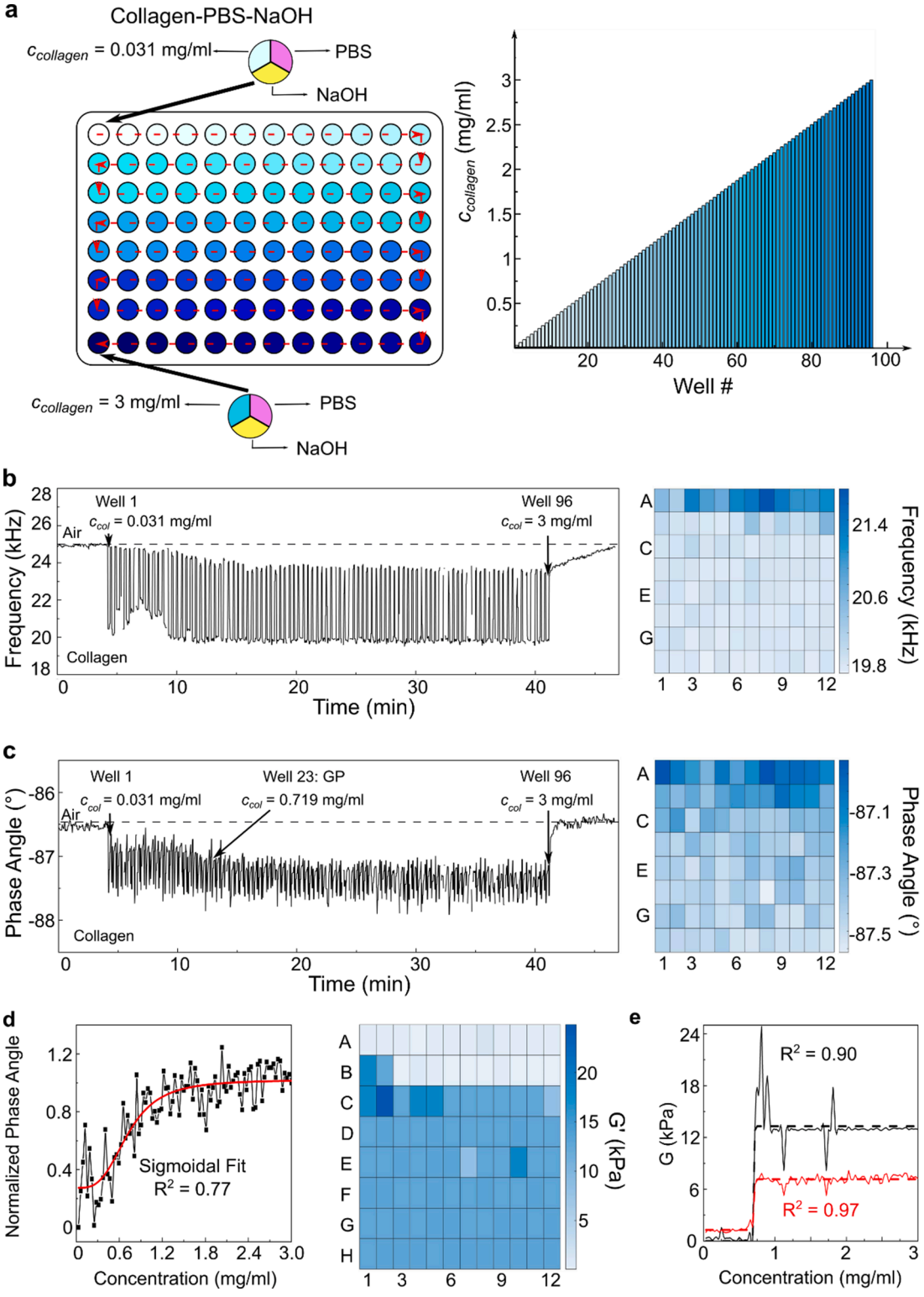

Fig. 5. **a)** Schematic of the sensor path and concentration distribution of a collagen hydrogel library in a 96-well plate format. Sensor resonant frequency (f) **(b)** and phase angle (ϕ) **(c)** responses associated with the measurement and corresponding heat maps. **d)** Plot of normalized phase angle vs. collagen concentration with a best-fit sigmoidal curve and rheological property heat maps of storage modulus (G') generated from sensor data and physics. **e)** Composition-property relations corresponding to the heat maps shown in **(d)** and the corresponding best-fit sigmoidal curves.

addition, all wells that contained a hydrogel were successfully characterized based on the criteria that the calculated $G' > G''$.

In addition to synthetic polymers (e.g., PF127 hydrogels), we next characterized hydrogel libraries of natural polymers to further demonstrate the utility and impact of the method. Collagen-based hydrogels have received considerable attention as scaffolds for tissue engineering applications. It is well established that the stiffness of two- and three-dimensional substrates and matrices for cell culture affect cellular behavior and tissue outcomes. For example, the design of processable hydrogels for neural tissue engineering applications remains an active

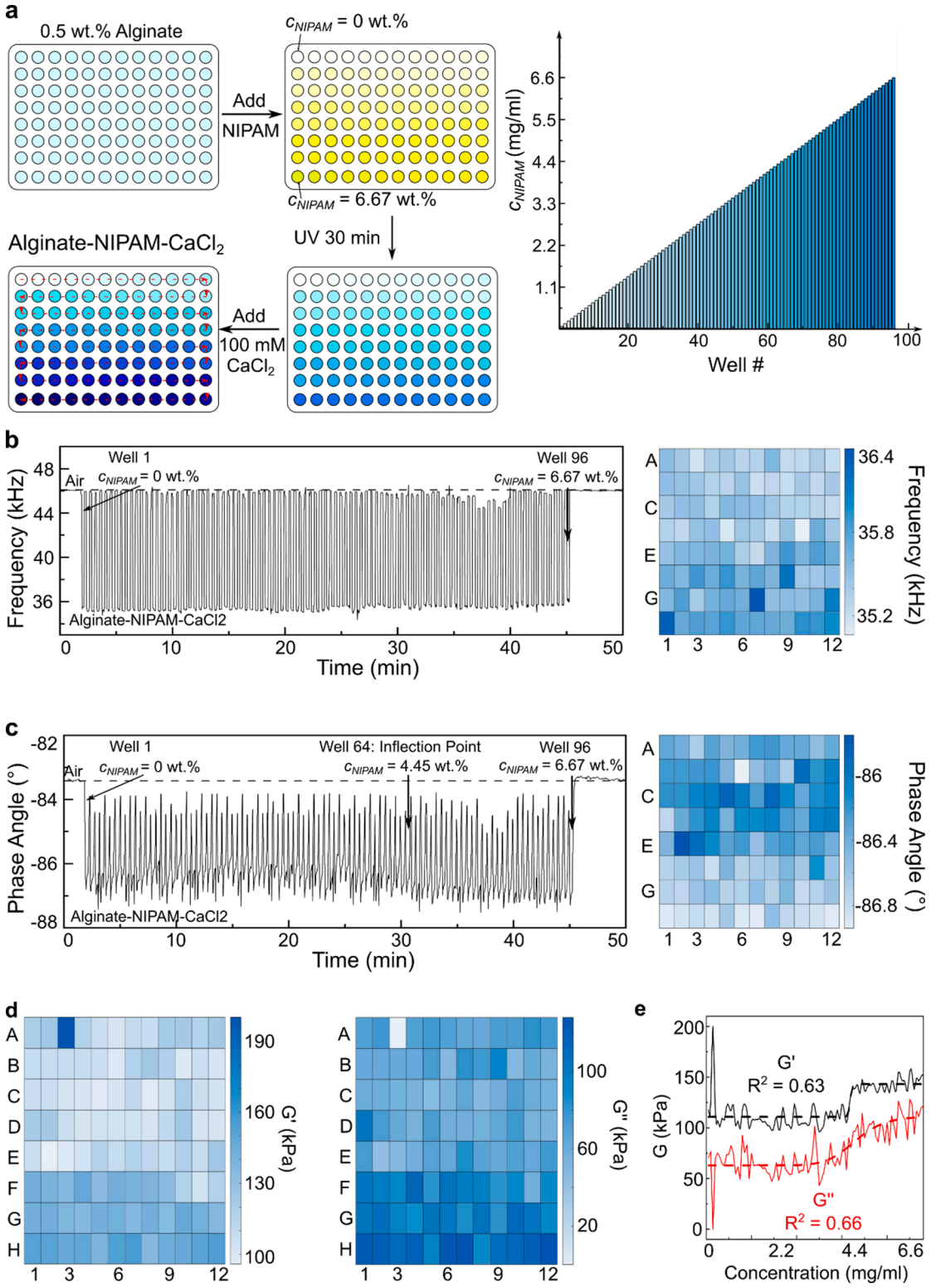

Fig. 6. a) Schematic of the sensor path and concentration distribution of a composite alginate-PNIPAM hydrogel library in a 96-well plate format. Sensor resonant frequency (f) **(b)** and phase angle (ϕ) **(c)** responses associated with the measurement and corresponding heat maps of steady-state responses. **d)** Rheological property heat maps of storage (G') and loss (G'') moduli generated from sensor data and physics. **e)** Composition-property relations corresponding to the heat maps shown in **(d)** and the best-fit sigmoidal curve.

area of research [43,44]. Thus, identifying the minimum polymer content needed to cause gelation could inform the design of future 'ultra-soft' tissue scaffolds. In addition, the optimization of the polymer content required to manufacture engineered tissues is also an important present economic and logistical consideration in tissue manufacturing, given the high cost and supply chain challenges.

As shown in Fig. 5a, we next characterized a 96-sample collagen hydrogel library that exhibited a linear concentration distribution with respect to collagen across the range of 0.031 to 3 mg/ml with a step size of 0.031 mg/ml. Similar to the PF127 hydrogel libraries discussed in Figs. 2 and 3, the concentration range spanned the known gel point (near 1 mg/ml) [45–47]. The ϕ and f responses and corresponding heat maps associated with the collagen library are shown in Fig. 5b and c. Similar to the PF127 hydrogel library, the steady-state ϕ response exhibited a sigmoidal trend. The gel point of the collagen hydrogel was obtained as 0.760 ± 0.048 mg/ml ($n = 3$ repeated studies) (see Fig. 5), which agreed well with previously reported estimates near, and also below, 1 mg/ml [45–47]. Considering the normalized ϕ response exhibited a strong correlation with the rheometer-measured property data from Fig. 3, the normalized ϕ response with respect to concentration and the rheological property heat map are shown in Fig. 5d. The composition-property relations associated with the sample library are shown in Fig. 5e.

In addition to characterizing hydrogel libraries that exhibit mechanical percolation processes associated with phase change (i.e., gelation), we next applied the method to identify the mechanical property percolation associated with network interaction in stimuli-responsive composite hydrogel libraries in which all samples were hydrogels. Composite alginate-PNIPAM hydrogels have received considerable attention based on their biocompatibility, mechanical strength, and thermal response [48]. Interpenetrating ionic and covalent networks can also result in tough alginate-PNIPAM hydrogels, which have been leveraged for soft robotics [49] and drug delivery applications [50,51]. However, the study of composition-process-structure-property relations remains an active research area. Fig. 6a shows the concentration distribution of reactants associated with the 96-sample alginate-PNIPAM hydrogel library and the associated sample preparation (synthesis) steps. The NIPAM concentration varied linearly across the library from 0 to 6.67 wt% with a step size of 0.069 wt%. Similar to the previous hydrogel libraries that exhibited a percolation in storage modulus associated with a gelation process, the f (Fig. 6b) and ϕ (Fig. 6c) responses and associated heat maps of steady-state sensor responses show a mechanical percolation process in the alginate-PNIPAM hydrogel library associated with network interaction. As shown in Fig. 6d and e, alginate-PNIPAM hydrogels undergo a percolation process at 4.68 ± 0.21 wt% NIPAM that drives sharp increase in G'. Following the percolation threshold, G' continues to increase, but at a lower rate than the rate of loss modulus increase, suggesting that the stimuli-responsive material becomes relatively more dissipative at NIPAM concentrations greater than 4.45 wt%.

Having established a rapid HTC method for generating composition-property relations for hydrogels from sensor data and sensor physics based on automated sensing, we next utilized these inputs in combination with supervised machine learning to create an autonomous HTC method capable of accurately interpreting the hydrogel composition-property characterization data, such as the ability to classify the sample's phase as solution or gel. The creation of autonomous HTC methods is also an important approach for increasing the speed (i.e., throughput), as data interpretation is often a significant bottleneck in materials research. As previously discussed (see Fig. 1), HTC methods can not only accelerate materials discovery by removing bottlenecks associated with screening of molecular and materials candidates, but they also generate data for facilitating and improving AI-guided modeling, synthesis, and characterization thrusts. We remind the reader that chemistry and materials applications of machine learning are presently physics-rich but data-poor, in part because of the absence of rapid HTC methods. While there are various problems in materials science and discovery, such as prediction of composition-property relations [52–54], here, we focus on the application of regression and supervised machine learning (classification) for deepening the understanding of hydrogel percolation physics based on the generated high-resolution experimental composition-property relations for large sample libraries as well as improving the accuracy of data interpretation. The data in Figs. 2c, 3e, and f (raw ϕ response, normalized ϕ response, low-frequency G' calculated from normalized ϕ response and rheometer data, and phase label) served as the inputs to the classification task. The novel HTC method generated high-resolution (i.e., dense) composition-property relation data for machine learning. For example, 1152 data samples were obtained from all of the repeated scans for the PF127 hydrogel studies, of which approximately 60% corresponded to the solution phase (class 0) and 40% to the gel phase (class 1). For modeling the supervised classification task, Support vector machine (SVM), Random forest (RF), and Extreme gradient boosting (XGB) classifiers were used based on their use as benchmarks in supervised machine learning and materials science applications [55–57].

As shown in Fig. 7a, raw ϕ response, normalized ϕ response, and low-frequency G' (obtained from normalized ϕ response and rheometer data) were strongly correlated (all absolute correlation scores exceeded 0.99). We found that default model parameters of SVM, RF, and XGB classifiers enabled classification accuracy greater than 96% (96.1, 100 and 96.1%, respectively). The associated computing times for model tuning and classification were 6, 42, and 30 s, respectively. Model tuning improved classification accuracy to greater than 96.5% (96.5, 100, and 99.57%, respectively) (see Table 1). A comparison of classifier performance for gelation and interaction network-driven percolation using raw ϕ response and characterization data from rheology studies is shown in Table 1. The high test accuracy, F1-score, precision, recall, and low misclassification error indicated that all three models performed comparably well for the classification of the hydrogel phase. Based on these metrics, XGB and RF classifiers provided similar performance to SVM. SVM provides optimal performance for relatively small datasets and typically works relatively well when there is a clear margin of separation between classes, such as a sharp phase transition point or percolation threshold. Thus, it was expected that SVM would provide an accurate classification of material phase based on sensor data. RF and XGB classifiers are known for relatively reduced overfitting and interpretability, given their basis on ensembles of decision trees.

The input features to the classification task were then further subdivided into sensor-based features, which included the raw ϕ response, normalized ϕ response, and low-frequency G' calculated from normalized ϕ response and rheometer data, and physics-based features, which included G' at f generated from raw sensor data and sensor physics. Fig. 7b shows the feature importance plots associated with the RF and XGB classifiers considering only the sensor-based features (i.e., obtained in the absence of sensor physics). Considering the PF127 hydrogel, the low-frequency G' calculated from the normalized ϕ response and rheometer data was the most important sensor-based feature for the RF and XGB classifiers. The normalized ϕ response was the second most important sensor-based feature for both classifiers. This result suggests that high classification accuracy of material phase can be achieved solely with features obtained from sensor data.

Having evaluated the relative importance of the sensor-based features obtained by the HTC method for different classifiers, we next compared the importance of the sensor- vs. physics-based features for a single classifier (see Table 2). As shown in Table 2, the RF classifier yielded accurate classification of percolation processes in PF127, collagen, and alginate-PNIPAM hydrogels using: 1) only a sensor-based feature (normalized ϕ response); 2) only a physics-based feature (G' at f); and 3) both features. As shown in Fig. 7c - e, the physics-based feature was more important than the sensor-based features for phase classification in the collagen and alginate-PNIPAM hydrogels. However, the ratio of feature importance was dependent on the type of material characterized, suggesting that the value of incorporating physics in machine learning may be material-dependent. Thus, considering the

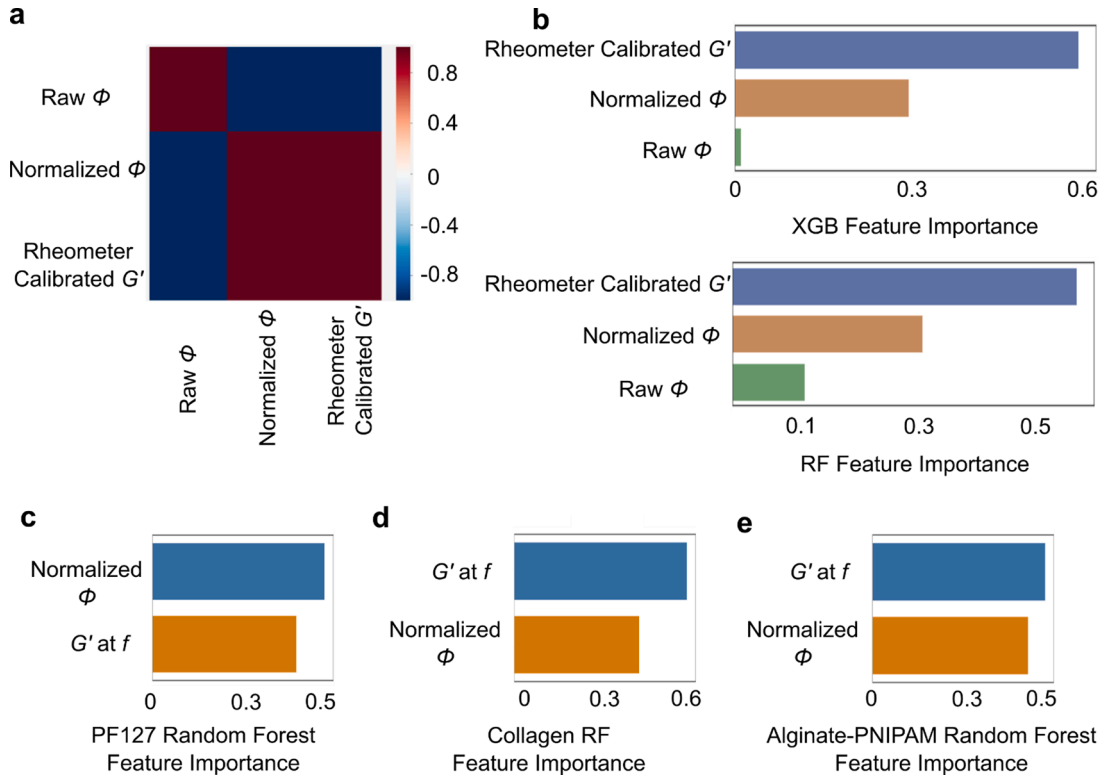

Fig. 7. a) Correlation matrix of input sensor-based features for the PF127 hydrogel library. **b)** Feature importance for RF and XGB classifiers for PF127 hydrogel phase classification. Feature importance for PF127 **(c)**, collagen **(d)**, and alginate-PNIPAM **(e)** hydrogel libraries using normalized steady-state phase angle (ϕ) response and G' at f in the RF classifier.

Table 1
Summary of model performance for classification of material phase using features obtained from sensor data (i.e., sensor-based features).

Model	Test Accuracy	Misclassification Error (%)	F1-score	Precision	Recall
SVM	0.965	3.5	0.96	0.96	0.97
XGB	0.996	0	1	0.99	1
RF	1	0	1	1	1

total characterization time was 0.39 min/sample and the computational time associated with supervised machine learning (i.e., phase classification) averaged ~ 30 s, the time-to-results associated with the method was ~24 s/sample.

In Table 3, we compare the established autonomous HTC method with state-of-the-art and gold-standard methods for characterizing hydrogel rheological properties, which include atomic force microscopes, rheometers, and dynamic mechanical analyzers. The method presented in this work, based on automated sensing and physics-guided machine learning, offers an improvement in the characterization cycle rate by reducing the process operation and handling times (e.g., sample preparation time). Finally, it is important to distinguish between automated methods capable of characterizing batches of samples vs. those that require manual loading, positioning, and unloading of samples by a trained user. Given sample mass and volume may be limited in many applications, such as materials discovery and sensing applications, it is also important to consider a method's minimum allowable sample volume. Autonomous HTC methods that are compatible with well plates, such as that presented in this work based on automated sensing and physics-guided machine learning, can characterize batches with a high quantity of samples, use low sample volume, and synergize with common HTE formats, which makes them attractive for HTE applications involving hydrogels and potentially other soft materials.

4. Conclusions

Autonomous methods for HTE offer the potential to improve the pace and reproducibility of scientific inquiry and quality control across various fields and industries. Here, we reported a rapid, autonomous method for HTC of hydrogels based on robotically-directed automated

Table 2
Summary of random forest (RF) model performance for classification of material phase for various material systems using sensor- (normalized ϕ response) and physics-based features (i.e., G' at f obtained from sensor data and physics).

Hydrogel	Feature(s)	Test Accuracy	F1-score	Precision	Recall	Misclassification Error (%)
Pluronic F127	ϕ/ϕ_{max}	0.965	0.97	0.96	0.96	3.45
Collagen	ϕ/ϕ_{max}	0.965	0.97	0.98	0.93	3.45
Alginate-PNIPAM	ϕ/ϕ_{max}	0.845	0.84	0.83	0.80	15.5
Pluronic F127	G'	1	1	1	1	0
Collagen	G'	1	1	1	1	0
Alginate-PNIPAM	G'	0.983	0.98	0.99	0.97	1.72
Pluronic F127	ϕ/ϕ_{max} & G'	1	1	1	1	0
Collagen	ϕ/ϕ_{max} & G'	1	1	1	1	0
Alginate-PNIPAM	G'	0.983	0.98	0.99	0.97	1.72

Table 3
Comparison of the gold-standard and state-of-the-art methods for characterization of rheological properties. The characterization cycle time is defined as the sum of the sample handling time (e.g., sample preparation time, time associated with sample-system integration and tool positioning), operation time (i.e., time for the measurement to occur after the sample has been prepared and the tool positioned), and tooling time (e.g., time required to clean or replace measurement fixtures or sensors).

	Rheometer	Dynamic Mechanical Analyzers	Atomic Force Microscopes	Autonomous Sensor-based HTC
Cycle Time (hr/sample)	1 [58]	0.5 – 24 [59]	0.5 [60]	0.0067
Cycle Rate (samples/hr)	2	~0.041- 2	2	150
Well Plate Compatible	No	No	No	Yes
Handling Method	Manual	Manual	Manual	Automated
Data Interpretation	Manual	Manual	Manual	Autonomous

sensing and physics-guided supervised machine learning. The method enables autonomous HTC of hydrogel rheological properties and high-resolution screening of gelation and percolation processes in 96-well plate formats at a rate of 24 s/sample (which is more than 70 times faster than the state-of-the-art methods), requiring no manual data analysis or interpretation. This work also shows that knowledge of sensor physics can improve the performance of autonomous HTC methods based on supervised machine learning via feature augmentation. Given the rheological properties of hydrogels are indicators of both processability and performance, the ability to rapidly and autonomously characterize the rheological properties of large batches of solutions and hydrogels in well plate formats is potentially meaningful for various applications, including accelerated materials discovery, sensing, tissue engineering, mechanobiology, and biomanufacturing. It is of interest to further consider how experimental data acquired from autonomous HTC methods can be utilized to guide material design (e.g., automated formulation processes) and how to further increase measurement speed and optimize the amount and type of sensor data collected (e.g., additional complementary composition, structure, and property data).

Data availability

The data that support the findings of this study are available from the corresponding author upon reasonable request.

CRediT authorship contribution statement

Junru Zhang: Conceptualization, Methodology, Software, Data curation, Formal analysis, Writing – original draft, Writing – review & editing. **Yang Liu:** Methodology, Writing – review & editing. **Durga Chandra Sekhar.P:** Methodology, Software, Formal analysis, Writing – original draft, Writing – review & editing. **Manjot Singh:** Methodology. **Yuxin Tong:** Methodology. **Ezgi Kucukdeger:** Methodology. **Hu Young Yoon:** Data curation. **Alexander P. Haring:** Conceptualization, Methodology. **Maren Roman:** Data curation, Writing – review & editing. **Zhenyu (James) Kong:** Writing – review & editing. **Blake N. Johnson:** Conceptualization, Methodology, Software, Formal analysis, Writing – original draft, Writing – review & editing.

Declaration of Competing Interest

The authors declare that they have no known competing financial interests or personal relationships that could have appeared to influence the work reported in this paper.

Data Availability

Data will be made available on request.

Acknowledgements

This work was supported by GlycoMIP, a National Science Foundation Materials Innovation Platform funded through Cooperative Agreement DMR-1933525. MR acknowledges support by the Virginia Agricultural Experiment Station and the Hatch Multistate Program of the National Institute of Food and Agriculture, U.S. Department of Agriculture. BNJ and ZK are also grateful for the support of the National Science Foundation (CMMI-1739318 & CBET-2144310). BNJ is also grateful for various discussions with Dr. Maneesh Gupta regarding high-throughput materials characterization.

Supplementary materials

Supplementary material associated with this article can be found, in the online version, at doi:10.1016/j.apmt.2022.101720.

References

[1] M.L. Green, C.L. Choi, J.R. Hattrick-Simpers, A.M. Joshi, I. Takeuchi, S.C. Barron, E. Campo, T. Chiang, S. Empedocles, J.M. Gregoire, A.G. Kusne, J. Martin, A. Mehta, K. Persson, Z. Trautt, J. Van Duren, A. Zakutayev, Fulfilling the promise of the materials genome initiative with high-throughput experimental methodologies, Appl. Phys. Rev. 4 (2017), 011105.
[2] J.J. de Pablo, N.E. Jackson, M.A. Webb, L.-Q. Chen, J.E. Moore, D. Morgan, R. Jacobs, T. Pollock, D.G. Schlom, E.S. Toberer, J. Analytis, I. Dabo, D. M. DeLongchamp, G.A. Fiete, G.M. Grason, G. Hautier, Y. Mo, K. Rajan, E.J. Reed, E. Rodriguez, V. Stevanovic, J. Suntivich, K. Thornton, J.-C. Zhao, New frontiers for the materials genome initiative, npj Comput. Mater. 5 (2019), 41.
[3] J. Seo, J.-Y. Shin, J. Leijten, O. Jeon, G. Camci-Unal, A.D. Dikina, K. Brinegar, A. M. Ghaemmaghami, E. Alsberg, A. Khademhosseini, High-throughput approaches for screening and analysis of cell behaviors, Biomaterials 153 (2018) 85–101.
[4] R.A. Potyrailo, I. Takeuchi, Role of high-throughput characterization tools in combinatorial materials science, Meas. Sci. Technol. 16 (2004) 1–4.
[5] A.Y. Anderson, Y. Bouhadana, H.-N. Barad, B. Kupfer, E. Rosh-Hodesh, H. Aviv, Y. R. Tischler, S. Rühle, A. Zaban, Quantum efficiency and bandgap analysis for combinatorial photovoltaics: sorting activity of Cu–O compounds in all-oxide device libraries, ACS Combinatorial Sci. 16 (2014) 53–65.
[6] D. Guevarra, A. Shinde, S.K. Suram, I.D. Sharp, F.M. Toma, J.A. Haber, J. M. Gregoire, Development of solar fuels photoanodes through combinatorial integration of Ni–La–Co–Ce oxide catalysts on BiVO4, Energy Environ. Sci. 9 (2016) 565–580.
[7] F. Xu, B. Corbett, S. Bell, C. Zhang, M. Budi Hartono, Z.J. Farsangi, J. MacGregor, T. Hoare, High-throughput synthesis, analysis, and optimization of injectable hydrogels for protein delivery, Biomacromolecules 21 (2020) 214–229.
[8] F. Soheilmoghaddam, M. Rumble, J. Cooper-White, High-throughput routes to biomaterials discovery, Chem. Rev. 121 (2021) 10792–10864.
[9] X. Zhang, Y. Xiang, Combinatorial approaches for high-throughput characterization of mechanical properties, J. Materiomics 3 (2017) 209–220.
[10] F. Ullah, M.B.H. Othman, F. Javed, Z. Ahmad, H.M. Akil, Classification, processing and application of hydrogels: a review, Mater. Sci. Eng.g: C 57 (2015) 414–433.
[11] L.J. White, C. Wark, L. Croucher, E.R. Draper, J.R. Hiscock, High-throughput characterisation of supramolecular gelation processes using a combination of optical density, fluorescence and UV-Vis absorption measurements, Chem. Commun. 56 (2020) 9557–9560.
[12] Z. Zhou, L. Ruiz Cantu, X. Chen, M.R. Alexander, C.J. Roberts, R. Hague, C. Tuck, D. Irvine, R. Wildman, High-throughput characterization of fluid properties to predict droplet ejection for three-dimensional inkjet printing formulations, Addit. Manuf. 29 (2019), 100792.
[13] M.S. Beal, B.E. Hayden, T. Le Gall, C.E. Lee, X. Lu, M. Mirsaneh, C. Mormiche, D. Pasero, D.C.A. Smith, A. Weld, C. Yada, S Yokoishi, High throughput methodology for synthesis, screening, and optimization of solid state lithium ion electrolytes, ACS Combinatorial Sci. 13 (2011) 375–381.
[14] M. Otani, K. Itaka, W. Wong-Ng, P.K. Schenck, H. Koinuma, Development of a high-throughput thermoelectric screening tool for combinatorial thin film libraries, Appl. Surf. Sci. 254 (2007) 765–767.
[15] M. Otani, N.D. Lowhorn, P.K. Schenck, W. Wong-Ng, M.L. Green, K. Itaka, H. Koinuma, A high-throughput thermoelectric power-factor screening tool for rapid construction of thermoelectric property diagrams, Appl. Phys. Lett. 91 (2007), 132102.

[16] P. Agarwal, H.-p. Lee, P. Smeriglio, F. Grandi, S. Goodman, O. Chaudhuri, N. Bhutani, A dysfunctional TRPV4–GSK3β pathway prevents osteoarthritic chondrocytes from sensing changes in extracellular matrix viscoelasticity, Nature Biomed. Eng. 5 (2021) 1472–1484.
[17] K. Lee, Y. Chen, X. Li, Y. Wang, N. Kawazoe, Y. Yang, G. Chen, Solution viscosity regulates chondrocyte proliferation and phenotype during 3D culture, J. Mater. Chem. B 7 (2019) 7713–7722.
[18] H.F. Brinson, L.C. Brinson, Polymer engineering science and viscoelasticity, An Introduction (2008).
[19] J.M. Zuidema, C.J. Rivet, R.J. Gilbert, F.A. Morrison, A protocol for rheological characterization of hydrogels for tissue engineering strategies, J. Biomed. Mater. Res. Part B: Appl. Biomater. 102 (2014) 1063–1073.
[20] J. Hutchinson, Plasticity at the micro scale, Int. J. Solids Struct. 37 (2000) 225–238.
[21] W.D. Nix, H. Gao, Indentation size effects in crystalline materials: a law for strain gradient plasticity, J. Mech. Phys. Solids 46 (1998) 411–425.
[22] M. Hardiman, T.J. Vaughan, C.T. McCarthy, A review of key developments and pertinent issues in nanoindentation testing of fibre reinforced plastic microstructures, Compos. Struct. 180 (2017) 782–798.
[23] M.L. Mather, M. Rides, C.R.G. Allen, P.E. Tomlins, Liquid viscoelasticity probed by a mesoscale piezoelectric bimorph cantilever, J. Rheol. 56 (2011) 99–112.
[24] Y. Nakano, I. Sato, Y. Seida, Y. Nakano, Viscoelastic behavior of thermoresponsive polymer hydrogel with organic adsorbate observed using quartz crystal microbalance, Chem. Lett. 36 (2007) 1204–1205.
[25] K. Sadman, C.G. Wiener, R.A. Weiss, C.C. White, K.R. Shull, B.D. Vogt, Quantitative rheometry of thin soft materials using the quartz crystal microbalance with dissipation, Anal. Chem. 90 (2018) 4079–4088.
[26] E.A. Corbin, L.J. Millet, J.H. Pikul, C.L. Johnson, J.G. Georgiadis, W.P. King, R. Bashir, Micromechanical properties of hydrogels measured with MEMS resonant sensors, Biomed. Microdevices 15 (2013) 311–319.
[27] Mutharasan, R., Xu, S., Johnson, B. N., Sharma, H. & Lakshmanan, R. S. Detection and measurement of mass change using an electromechanical resonator United States patent (2010).
[28] E. Cesewski, M. Singh, Y. Liu, J. Zhang, A.P. Haring, B.N. Johnson, Real-time monitoring of hydrogel rheological property changes and gelation processes using high-order modes of cantilever sensors, J. Appl. Phys. 128 (2020), 174502.
[29] A.P. Haring, M. Singh, M. Koh, E. Cesewski, D.A. Dillard, Z.J. Kong, B.N. Johnson, Real-time characterization of hydrogel viscoelastic properties and sol-gel phase transitions using cantilever sensors, J. Rheol. 64 (2020) 837–850.
[30] M. Singh, J. Zhang, K. Bethel, Y. Liu, E.M. Davis, H. Zeng, Z. Kong, B.N. Johnson, Closed-loop controlled photopolymerization of hydrogels, ACS Appl. Mater. Interfaces 13 (2021) 40365–40378.
[31] B.N. Johnson, R. Mutharasan, A novel experimental technique for determining node location in resonant mode cantilevers, J. Micromech. Microeng. 21 (2011), 065027.
[32] B.N. Johnson, H. Sharma, R. Mutharasan, Torsional and lateral resonant modes of cantilevers as biosensors: alternatives to bending modes, Anal. Chem. 85 (2013) 1760–1766.
[33] B.N. Johnson, R. Mutharasan, Persistence of bending and torsional modes in piezoelectric-excited millimeter-sized cantilever (PEMC) sensors in viscous liquids - 1 to 103 cP, J. Appl. Phys. 109 (2011), 066105.
[34] B.N. Johnson, R. Mutharasan, The origin of low-order and high-order impedance-coupled resonant modes in piezoelectric-excited millimeter-sized cantilever (PEMC) sensors: experiments and finite element models, Sens. Actuators B 155 (2011) 868–877.
[35] B.N. Johnson, R. Mutharasan, Electrochemical piezoelectric-excited millimeter-sized cantilever (ePEMC) for simultaneous dual transduction biosensing, Analyst 138 (2013) 6365–6371.
[36] Mutharasan, R., Xu, S., Johnson, B. N., Sharma, H. & Lakshmanan, R. S. (Google Patents, 2014).
[37] H. Sharma, R.S. Lakshmanan, B.N. Johnson, R. Mutharasan, Piezoelectric cantilever sensors with asymmetric anchor exhibit picogram sensitivity in liquids, Sens. Actuators B 153 (2011) 64–70.
[38] T. Itoh, C. Lee, T. Suga, Deflection detection and feedback actuation using a self-excited piezoelectric Pb (Zr, Ti) O3 microcantilever for dynamic scanning force microscopy, Appl. Phys. Lett. 69 (1996) 2036–2038.
[39] T. Itoh, T. Suga, Self-excited force-sensing microcantilevers with piezoelectric thin films for dynamic scanning force microscopy, Sens. Actuators, A 54 (1996) 477–481.
[40] C.A. Van Eysden, J.E. Sader, Frequency response of cantilever beams immersed in compressible fluids with applications to the atomic force microscope, J. Appl. Phys. 106 (2009), 094904.
[41] G. Kemmer, S. Keller, Nonlinear least-squares data fitting in Excel spreadsheets, Nat. Protoc. 5 (2010) 267–281.
[42] C. Chaibundit, N.M.P.S. Ricardo, F.d.M.L.L. Costa, S.G. Yeates, C. Booth, Micellization and gelation of mixed copolymers P123 and F127 in aqueous solution, Langmuir 23 (2007) 9229–9236.
[43] A.P. Haring, H. Sontheimer, B.N. Johnson, Microphysiological human brain and neural systems-on-a-chip: potential alternatives to small animal models and emerging platforms for drug discovery and personalized medicine, Stem Cell Rev. Rep. 13 (2017) 381–406.
[44] A.P. Haring, E.G. Thompson, Y. Tong, S. Laheri, E. Cesewski, H. Sontheimer, B. N. Johnson, Process- and bio-inspired hydrogels for 3D bioprinting of soft free-standing neural and glial tissues, Biofabrication 11 (2019), 025009.
[45] F.H.M. Nestler, S. Hvidt, J.D. Ferry, A. Veis, Flexibility of collagen determined from dilute solution viscoelastic measurements, Biopolymers 22 (1983) 1747–1758.
[46] M. Shayegan, N.R. Forde, Microrheological characterization of collagen systems: from molecular solutions to fibrillar gels, PLoS One 8 (2013), e70590.
[47] Y.-l. Yang, L.M. Leone, L.J. Kaufman, Elastic moduli of collagen gels can be predicted from two-dimensional confocal microscopy, Biophys. J. 97 (2009) 2051–2060.
[48] M. Ochi, J. Ida, T. Matsuyama, H. Yamamoto, Effect of synthesis temperature on characteristics of PNIPAM/alginate IPN hydrogel beads, J. Appl. Polym. Sci. 132 (2015).
[49] W.J. Zheng, N. An, J.H. Yang, J. Zhou, Y.M. Chen, Tough Al-alginate/Poly(N-isopropylacrylamide) hydrogel with tunable LCST for soft robotics, ACS Appl. Mater. Interfaces 7 (2015) 1758–1764.
[50] J.-H. Choi, H.Y. Lee, J.-C. Kim, Release behavior of freeze-dried alginate beads containing poly(N-isopropylacrylamide) copolymers, J. Appl. Polym. Sci. 110 (2008) 117–123.
[51] F. Rezaei, S. Damoogh, R.L. Reis, S.C. Kundu, F. Mottaghitalab, M. Farokhi, Dual drug delivery system based on pH-sensitive silk fibroin/alginate nanoparticles entrapped in PNIPAM hydrogel for treating severe infected burn wound, Biofabrication 13 (2020), 015005.
[52] A. Fluegel, A.K. Varshneya, D.A. Earl, T.P. Seward, D. Oksoy, Improved composition-property relations in silicate glasses, part I: viscosity, Ceram. Trans. 170 (2005) 129–143.
[53] L. Kiri, D. Boyd, Predicting composition–property relationships for glass ionomer cements: a multifactor central composite approach to material optimization, J. Mech. Behav. Biomed. Mater. 46 (2015) 285–291.
[54] X. Shi, H. Li, Z. Song, X. Zhang, G. Liu, Quantitative composition-property relationship of aviation hydrocarbon fuel based on comprehensive two-dimensional gas chromatography with mass spectrometry and flame ionization detector, Fuel 200 (2017) 395–406.
[55] J. Cai, X. Chu, K. Xu, H. Li, J. Wei, Machine learning-driven new material discovery, Nanoscale Adv. 2 (2020) 3115–3130.
[56] H. Nguyen, T. Vu, T.P. Vo, H.-T. Thai, Efficient machine learning models for prediction of concrete strengths, Constr. Build. Mater. 266 (2021), 120950.
[57] J. Wei, X. Chu, X.-Y. Sun, K. Xu, H.-X. Deng, J. Chen, Z. Wei, M. Lei, Machine learning in materials science, InfoMat 1 (2019) 338–358.
[58] A. Shenoy, Nonrecovered compliance from dynamic oscillatory test vis-à-vis nonrecovered compliance from multiple stress creep recovery test in the dynamic shear rheometer, Int. J. Pavement Eng. 9 (2008) 329–341.
[59] D. Ionita, M. Cristea, C. Gaina, Prediction of polyurethane behaviour via time-temperature superposition: meanings and limitations, Polym. Test. 83 (2020), 106340.
[60] R. Foschia, M. Jobin, S. Hengsberger, Local dynamic mechanical analysis, Micron 40 (2009) 51–55.